

Effective Maximum Likelihood Grid Map With Conflict Evaluation Filter Using Sonar Sensors

Kyoungmin Lee and Wan Kyun Chung, *Member, IEEE*

Abstract—In this paper, we address the problem of building a grid map using cheap sonar sensors, i.e., the problem of using erroneous sensors when seeking to model an environment as accurately as possible. We rely on the inconsistency of information among sonar measurements and the sound pressure of the waves from the sonar sensors to develop a new method of detecting incorrect sonar readings, which is called the conflict evaluation with sound pressure (CEsp). To fuse the correct measurements into a map, we start with the maximum likelihood (ML) approach due to its ability to manage the angular uncertainty of sonar sensors. However, since this approach suffers from heavy computational complexity, we convert it to a light logic problem called the maximum approximated likelihood (MAL) approach. Integrating the MAL approach with the CEsp method results in the conflict evaluated maximum approximated likelihood (CEMAL) approach. The CEMAL approach generates a very accurate map that is close to the map that would be built by accurate laser sensors and does not require adjustment of parameters for various environments.

Index Terms—Grid map, maximum likelihood (ML), sonar sensors.

I. INTRODUCTION

THE GRID map, which is a discretized field that converts an environment into a spatial lattice [1], is extremely easy to recognize and understand and can be used for localization [2], path planning [3], collision avoidance [4], interaction between humans and robots [5], and multisensor fusion [6]. Various methods of range measurement have been used to build grid maps, including laser range finders (LRFs), cameras, and sonar sensors. Although LRFs are attractive in terms of accuracy, a

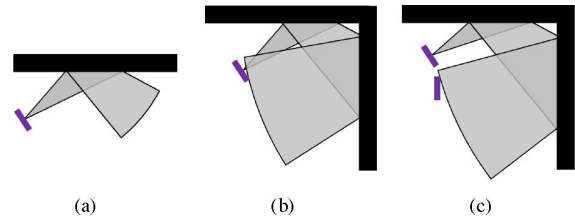


Fig. 1. Examples of undesirable reflections. (a) Mirror-like reflection occurs when the emitted wave is obliquely reflected from smooth surfaces [10]. (b) High-order reflection occurs when the wave returns after striking multiple obstacles [12]. (c) Crosstalk occurs when the wave returns to a different sensor [13].

laser beam penetrates glass objects [7]. Cameras are sensitive to the illumination level [8]. Sonar sensors are designed to measure the range to the closest obstacle in their beamwidth and are not subject to problems of penetration or sensitivity to illumination. Furthermore, since sonar sensors are much less expensive than LRFs,¹ they are attractive for practical indoor service robots, such as a robotic vacuum cleaner.

Despite their advantages, sonar sensors suffer from two well-known characteristic problems: incorrect measurements and angular uncertainty.

- 1) *Incorrect measurements*: Sonar sensors frequently fail to detect the nearest obstacle because of undesirable reflections (see Fig. 1). A reflection causes an incorrect reading that can form ghost obstacles or omit real obstacles from the map. Experiments in general indoor environments have shown that about more than half of sonar measurements are spurious. This will be described in detail in Section IV.
- 2) *Angular uncertainty*: Sonar sensors directly provide range information about the nearest obstacle but not angular information [9]. The uncertainty can hide narrow openings [10], [11] and distort the map.

Under these problems, we propose a new grid-mapping method called the conflict evaluated maximum approximated likelihood (CEMAL) approach. It starts with the maximum likelihood (ML) approach due to its effectiveness for managing angular uncertainty [11]. Despite this advantage, however, the ML approach has two drawbacks: erroneous maps (the map that contain ghost obstacles or fail to show real obstacles due to the effects of incorrect measurements) and a heavy computational load (the computational complexity of the ML approach is $O(2^k n)$, where k is the number of cells, and n is the number of sonar readings).

We have found that *conflict cells*, which will be presented in detail in Section III, are related to these side effects as follows.

Manuscript received August 24, 2008; revised February 10, 2009. First published July 6, 2009; current version published July 31, 2009. This paper was recommended for publication by Associate Editor A. Martinelli and Editor L. Parker upon evaluation of the reviewers' comments. This work was supported in part by the Acceleration Research Program of the Ministry of Education, Science, and Technology of the Republic of Korea and the Korea Science and Engineering Foundation (R17-2008-021-01000-0), in part by the Korea Health 21 R&D Project, Ministry of Health and Welfare, Republic of Korea, under Grant A020603, in part by the Agency for Defence Development and by Unmanned Technology Research Center, Korea Advanced Institute of Science and Technology, in part by the Korea Science and Engineering Foundation under Korea Government Grant MOST R0A-2003-000-10308-0, and in part by the IT R&D Program of Ministry of Knowledge and Economy (MKE)/Institute for Information Technology Advancement (IITA) (2008-F-038-1, Development of Context Adaptive Cognition Technology).

The authors are with the Department of Mechanical Engineering, Pohang University of Science and Technology, 790-784 Pohang, Korea (e-mail: lekomin@postech.ac.kr; wkchung@postech.ac.kr).

This paper has supplementary downloadable multimedia material available at <http://ieeexplore.ieee.org>, provided by the author. This material includes one video (CEMAL.mpg) that contains grid mapping procedure using the CEMAL approach. In order to play the multimedia file, Microsoft's Windows media player 9.0 is required minimally. The size is 28 MB. Contact lekomin@postech.ac.kr for further questions about this work.

Color versions of one or more of the figures in this paper are available online at <http://ieeexplore.ieee.org>.

Digital Object Identifier 10.1109/TRO.2009.2024783

¹The cost of the MA40B8 sonar sensor from Murata Company, Ltd., is about \$3, while that of a typical LRF, such as URG-04LX from Hokuyo Company, Ltd., is about \$2000.

- 1) *Erroneous map*: As conflict cells are caused only by incorrect measurements, it is essential to remove them. To do this, we propose the conflict evaluation with sound pressure (CEsp) method, which distinguishes the incorrect readings that cause conflict cells. The incorrect readings are filtered using the CEsp method, and then, the erroneous parts can be reduced.
- 2) *Heavy computational load*: When there are no conflict cells, the ML approach can be converted to a simple logic process that has light $O(n)$ computational complexity by an approximation of the likelihood. This is the maximum approximated likelihood (MAL) approach.

The CEMAL approach thus consists of two layers: the filtering layer (CEsp method) and the fusion layer (MAL approach). When conflict cells occur, the CEsp method detects incorrect readings. Only the correct readings are fused into a grid map using the MAL approach. Our main contributions are as follows.

- 1) CEMAL inherits the angular uncertainty handling capability of the ML approach. Unlike the ML approach, however, CEMAL eliminates erroneous parts because the CEsp method filters them out. Therefore, the quality of a CEMAL grid map is excellent even using cheap sonar sensors. Based on two criteria given in Section VI, we confirmed that the CEMAL grid map is about 92% accurate and that it can represent about 96% of an environment.
- 2) CEMAL has a light $O(n)$ computational load that is comparable to the previous binary or trinary estimation approaches [1], [14]–[24] and is very low compared with the $O(2^k n)$ load of the ML approach. In addition, it can work incrementally. Several experiments showed that CEMAL requires approximately 1 ms to process one measurement.
- 3) CEMAL does not require adjustment of parameters. Binary or trinary estimation approaches must regulate their own updating parameters carefully to establish an accurate map. CEMAL requires partial modification only when using a different kind of sonar sensor.
- 4) CEMAL works well even with only two sonar sensors. The possibility of using a low number of sonar sensors allows CEMAL to be used in commercial applications.

The remainder of the paper is organized as follows. We begin by describing related research in Section II. Conflict cells, which are the key for overcoming the problems of the ML approach, and the CEsp method are described in Section III. Descriptions of the MAL approach are presented in Section IV. Section V summarizes the characteristics of the CEMAL approach. Experimental results are given in Section VI, and Section VII presents the summary and conclusions.

II. RELATED RESEARCHES

A. Grid Mapping

Previous grid-mapping approaches can be classified into two categories: binary (or trinary) estimation and high-dimensional optimization.

1) *Binary (or Trinary) Estimation*: As finding a solution among the 2^k possible maps is an intractable problem, binary or trinary estimation approaches decompose the high-dimensional

problem into a collection of binary or trinary state estimation problems based on the assumption that each cell is independent of the others [1]. The posterior approach (PT) [1], [14]–[16] calculates a posterior probability that measures the occupancy of the cell. Other approaches [17], [18] use a center-line model of the sonar sensor, and rely on the number of empty or occupied observations to estimate the state of each cell. The Dempster–Shafer approach (DS) [14], [19]–[21] infers a mass function that indicates whether a cell is occupied, empty, or in an unknown state based on the DS theory [25]. The fuzzy approach (FZ) [14], [22]–[24], which is based on the theory of fuzzy sets [26], quantifies the possibility that indicates a cell belongs to an obstacle and then determines safe cells that are free from obstacles. As these approaches explicitly or implicitly assume independence, they reduce the enormous computational burden and the computational complexity to $O(n)$. Because a measurement requires a constant time, the complexity is linear with the total number of measurements. However, the resulting grid map is defective in terms of representing narrow openings because the angular uncertainty is not handled appropriately by the assumption of the independence. Furthermore, these approaches require a tuning process whereby the updating parameters are regulated to acquire an accurate map.

2) *High-Dimensional Optimization*: Unlike the aforementioned approaches, the ML approach [11], [27] uses a likelihood of sensor measurements without the assumption of the independence of other cells, and acquires a grid map that maximizes this likelihood. As the ML approach suffers from a heavy computational load, the expectation–maximization (EM) algorithm [28] is used in [11]. This solution reduces the computational complexity to $O(nk)$ per iteration due to $O(n)$ for E -step and $O(nk)$ for M -step. The expectation of each measurement is calculated for the E -step, while for the M -step, the state of each cell is reversed, and the change in expectation of related measurements is examined. However, the number of iterations of the EM tends to depend linearly on the size of the search space 2^k for the worst case. In addition, the EM algorithm may fall into a local minimum and cannot process data incrementally.

B. Coping With Sonar Sensor Characteristics

Aside from mapping, previous research on methods for coping with the characteristics of sonar sensors can be divided into two groups. The first considered handling of the angular uncertainty of sonar sensors, and the second considered the detection of incorrect measurements.

1) *Handling Angular Uncertainty*: Arc maps [29] have been developed to deal with the angular uncertainty. The arc map shows an environment with only a collection of arcs, and obstacles can be located anywhere on the arcs. The arc-transversal median (ATM) method [9] gathers intersections of sonar arcs and extracts the median points from them. The arc-carving (AC) method [7] eliminates portions of sonar arcs that are contradicted by subsequent sonar readings and derives the mean point of the remaining arc. The directional maximum (DM) method [30] uses a direction of interest, and a cell that has a maximum intersection count along this direction is selected.

2) *Detecting Incorrect Measurements*: Several techniques have been developed for filtering out incorrect measurements, and these can be divided into four classes.

The first class eliminates incorrect sonar measurements by clustering. The random sample consensus/Gaussian filtering (RANSAC/GF) method [31] establishes a Gaussian distribution with the RANSAC clustering [32]; readings that do not fit the distribution are rejected as outliers.

The second class discriminates sonar measurements that form geometric primitives such as lines and points. The region of constant depth (RCD) matching method [33], [34] uses a geometric constraint based on the radius of a circle. Only sonar readings that satisfy this constraint are considered correct. The RCD matching method is useful for finding corners, planes, and cylinders. The feature-prediction (FP) method [35] assigns a confidence measure to each sonar reading to indicate whether it is reliable. The position and orientation of features established by hypothetical obstacles in the local space of the robot determine the reliability.

The third class limits the maximum admissible range adaptively. The bounding box method [36] was introduced to correct unreliable sonar sensor readings, thus creating a bounding box from four (front, back, left, and right) directional sensor readings. If a sensor reading falls outside the box, its range is modified to be on the border of the box. In the navigable Voronoi diagram (NVD) method [37], the diagram is generated by instantaneous measurements, and sonar readings beyond the diagram are excluded.

The fourth class focuses on the consistency of sonar information. The sonar probabilistic analysis of conflicts (spACs) method [38] iteratively determines the probability of each sonar reading based on the occurrence of conflict cells. The CEsp method is included in this class and will be described in the next section. The conflict evaluation method based on a logical approach was proposed [39] in precursor research into the CEsp method. However, because the previous approach has exceptional cases, it is difficult to apply generally.

III. CONFLICT EVALUATION METHOD

The inconsistency of information in cells can be a clue that indicates candidates for incorrect measurements, and the sound pressure of the wave from the sonar sensor determines incorrect readings among them.

A. Conflict Cells

A sonar measurement is divided into two regions: the arc region and the free region. The arc region is the farthest area of measurement where the cells are marked as occupied because obstacles are probably located there. The cells in the free region, which comprise everything within the beamwidth of the sensor except the arc region, are generally marked as empty as the free region is free of obstacles. Fig. 2 shows each region on a gridded field.

When multiple sonar measurements overlap, inconsistency of information contained in cells may occur. Depending on inconsistency, a cell is classified into two groups: the consistent cells

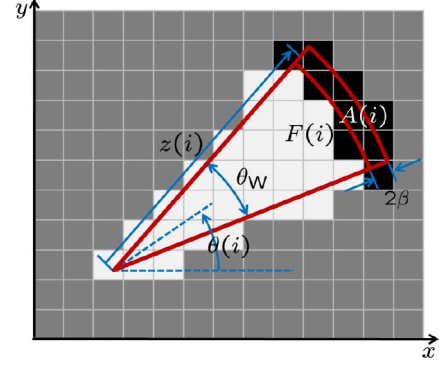


Fig. 2. Region of sonar reading i where $\theta(i)$ is the line of sight of the sensor, θ_w is the beamwidth, $z(i)$ is the range, $F(i)$ is the free region (white cells), $A(i)$ is the arc region (black cells), and 2β is the interval corresponding to range uncertainty.

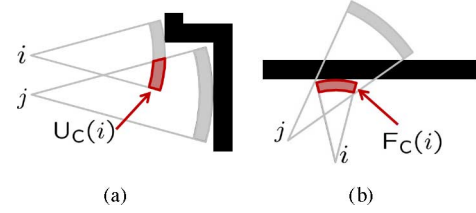


Fig. 3. Different types of inconsistent cell. (a) Uncertain cells (U_c). (b) Conflict cells (F_c).

(C_c) and the inconsistent cells (I_c). Inconsistent cells in the arc region of reading i are defined as

$$I_c(i) = \bigcup_{k=I(i)} (A(i) \cap F(k)) \quad (1)$$

where $A(i)$ and $F(k)$ are described in Fig. 2, and $I(i)$ is the index of sonar readings that each free region shares with the arc region of reading i . $I(i)$ is defined as

$$I(i) = \{k | A(i) \cap F(k) \neq \emptyset \text{ for } 1 \leq k \leq n (k \neq i)\} \quad (2)$$

where n is the total number of sonar readings. Unlike inconsistent cells, consistent cells are cells that contain only one type of information.

Inconsistent cells are classified into two groups: the uncertain cells [see Fig. 3(a)] and the conflict cells [see Fig. 3(b)]. When some arc cells are inconsistent, these inconsistent cells are classified as uncertain cells (U_c). In addition, when all of the arc cells are inconsistent, they are classified as conflict cells (F_c). Each cell is defined as follows:

$$U_c(i) = \{I_c(i) \text{ for } A(i) \neq I_c(i)\} \quad (3)$$

$$F_c(i) = \{I_c(i) \text{ for } A(i) = I_c(i)\}. \quad (4)$$

Eventually, the aforementioned classification can be summarized as Fig. 4.

It can be easily guessed that consistent and uncertain cells are caused by both correct and incorrect readings. For example, in Fig. 3(a), both i and j are correct, and thus, the uncertain cells $U_c(i)$ exist. Thus, candidates for incorrect readings cannot be obtained from consistent and uncertain cells. Unlike them,

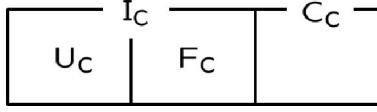


Fig. 4. Cell is in one of above groups.

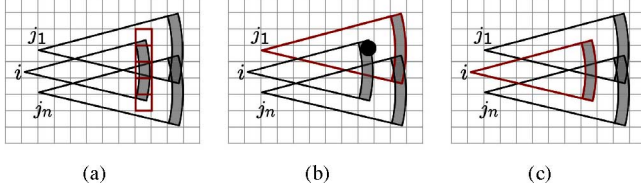


Fig. 5. (a) Conflict cells. (b) If we assume that an obstacle is located in the conflict cells, some sonar readings among $j_1 \cdots j_n$ will be incorrect. (c) Sonar reading i will be incorrect if we assume that there are no obstacles in the conflict cell area.

since conflict cells are always caused by incorrect sonar readings, as indicated by the following theorem, we can acquire the candidates.

Theorem 1: Conflict cells are caused only by incorrect readings.

Proof: Let us assume that conflict cells occur, as shown in Fig. 5(a). Without any loss of generality, we assume that conflict cells of sonar reading i occur along with several other readings $j_1 \cdots j_n$, i.e., $\# [I(i)] \geq 1$. If we assume that an obstacle is in the region where conflict cells occur, then some sonar readings among $j_1 \cdots j_n$ will be incorrect. Sonar reading j_1 in Fig. 5(b) is incorrect as the obstacle is in the free region of j_1 . In addition, if we assume that there are no obstacles in the region where conflict cells occur, then the sonar reading i will be incorrect as there is nothing in the arc region of i , as shown in Fig. 5(c). Therefore, conflict cells are always caused only by incorrect readings. ■

Theorem 1 indicates that incorrect readings are the only source of conflict cells. Therefore, when conflict cells occur, candidates for incorrect measurements can be obtained. In the case of Fig. 5(a), sonar readings i, j_1 and j_n become the candidates.

B. Conflict Evaluation Method

To determine incorrect readings among aforementioned candidates, we use the sound pressure of the wave from the sonar sensor.

1) *Sound Pressure:* The sound pressure of the transmitted wave is expressed as $SP_T(r, \theta)$, where r is the distance from the sensor to the obstacle and θ is the angle from the heading of the sensor. When $\theta = 0$, $SP_T(r, 0)$ can be approximated as

$$SP_T(r, 0) = 2\rho cU \left| \sin \left\{ \frac{1}{2}kr \left[\sqrt{1 + \left(\frac{a}{r}\right)^2} - 1 \right] \right\} \right| \quad (5)$$

$$\approx \frac{1}{2} \frac{\rho c U a^2 k}{r} \quad (6)$$

$$= \frac{c_1}{r} \quad (7)$$

where ρ is the density of the air, c is the sound speed in air, U is the speed of vibration of the circular piston inside the sonar sensor, k is the wavenumber, and a is the radius of the circular piston. Because a sonar sensor is often modeled as a plane circular piston [10], the sound pressure is expressed by (5) with more details provided in [40]. The far-field approximation ($r/a \gg 1$) [40] produces (6), and merging constant terms reduces this to (7). Equation (7) indicates that the sound pressure of the transmitted wave along the axis of its direction is approximately inversely proportional to r .

The transmitting directivity (D_T) or the directivity pattern [10] is required when considering the sound pressure of the transmitted wave off the axis of its direction, which is defined as

$$D_T(\theta) = 20 \log \left(\frac{SP_T(r, \theta)}{SP_T(r, 0)} \right). \quad (8)$$

From (7) and (8), the sound pressure of the wave off the axis θ can be expressed as

$$SP_T(r, \theta) = SP_T(r, 0) 10^{D_T(\theta)/20}. \quad (9)$$

The wave returns to the sensor after impinging on an obstacle located at (r, θ) . As the wave travels a distance of $2r$, the sound pressure $SP'_R(r, \theta)$ just before the sonar sensor receives the wave, which can be expressed as

$$SP'_R(r, \theta) = SP_T(2r, 0) 10^{D_T(\theta)/20}. \quad (10)$$

In a general indoor environment, a decrease due to the impingement against the obstacle frequently occurs. As the decrease is proportional to the reflection coefficient, which is constant for an obstacle of a specific material [40], we set it as an unknown constant c_2 . Thus, (10) becomes

$$SP'_R(r, \theta) = c_2 SP_T(2r, 0) 10^{D_T(\theta)/20}. \quad (11)$$

As the returning wave is off the axis θ , the sound pressure finally detected at the sensor is decreased as a function of the receiving directivity (D_R) or the sensitivity pattern [10], and the final detected sound pressure $SP_R(r, \theta)$ can be expressed as

$$SP_R(r, \theta) = c_2 SP_T(2r, 0) 10^{D_T(\theta)/20} 10^{D_R(\theta)/20} \quad (12)$$

$$= \frac{c_3}{r} 10^{(D_T(\theta) + D_R(\theta))/20}. \quad (13)$$

Although c_3 is an unknown constant in (13), it is not necessary to consider it because it is canceled when we compare sound pressure levels. Two terms $D_T(\theta)$ and $D_R(\theta)$ are required to derive the final detected sound pressure. For the purposes of this study, we investigated the directivity of the 600 series sensors (S600) from SensComp, Inc., and the MA40B8 sensors from Murata Company, Ltd. The MA40B8 is a piezoelectric transducer with a wider beamwidth and a lower cost than the S600 electrostatic transducer. Detailed properties of piezoelectric and electrostatic transducers are given in [10].

1) *S600:* As the S600 consists of just one module, D_T and D_R are the same. The directivity shown in Fig. 6(a) is from the manufacturer's data sheet. As we are only interested in a beamwidth of 22.5° , the directivity in the region of interest

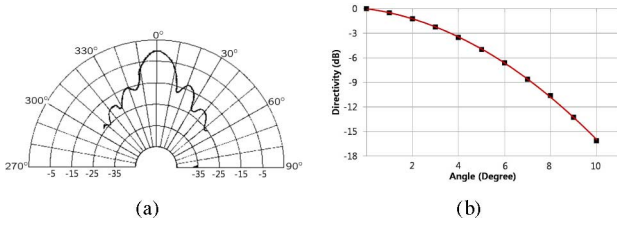


Fig. 6. (a) S600 directivity. (b) Approximate directivity in the region of interest. The squares were obtained from sampling in (a), and the solid line represents an approximated second-order polynomial.

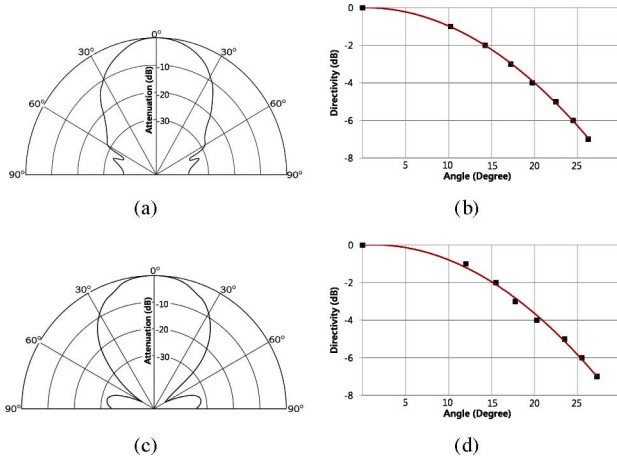


Fig. 7. (a) MA40B8 transmitter directivity. (b) Approximate transmitter directivity in the region of interest. (c) MA50B8 receiver directivity. (d) Approximate receiver directivity in the region of interest. In (b) and (d), squares were obtained from sampling the curves in (a) and (c), respectively. The solid lines in (b) and (d) indicate the approximated second-order polynomials.

can be approximated by a second-order polynomial, as shown in Fig. 6(b), using the following equation:

$$D_T(\theta) = D_R(\theta) \approx -0.0605\theta^2 - 0.1977|\theta| \quad \text{for } |\theta| \leq 11.25^\circ. \quad (14)$$

Eventually, when an obstacle is located in a cell (r, θ) relative to the sensor, the sound pressure recognized by the S600 is shown in Fig. 8(a), and its equation is given as

$$SP_R(r, \theta) = \frac{c_3}{r} 10^{(-0.00605\theta^2 - 0.01977|\theta|)}. \quad (15)$$

- 2) **MA40B8**: MA40B8 has both a transmitter and a receiver with directivities shown in Fig. 7(a) and (c), respectively. As the half-power beamwidth is about 45° , the directivity in the region of interest can be approximated by second-order polynomials, as shown in Fig. 7(b) and (d), using the following equations:

$$\left. \begin{aligned} D_T(\theta) &\approx -0.0103\theta^2 + 0.0053|\theta| \\ D_R(\theta) &\approx -0.0102\theta^2 + 0.0241|\theta| \end{aligned} \right\}, \quad \text{for } |\theta| \leq 22.5^\circ. \quad (16)$$

Based on these equations, the sound pressure recognized by the sonar sensor is shown in Fig. 8(b), and its equation is given by

$$SP_R(r, \theta) = \frac{c_3}{r} 10^{(-0.001025\theta^2 + 0.00147|\theta|)}. \quad (17)$$

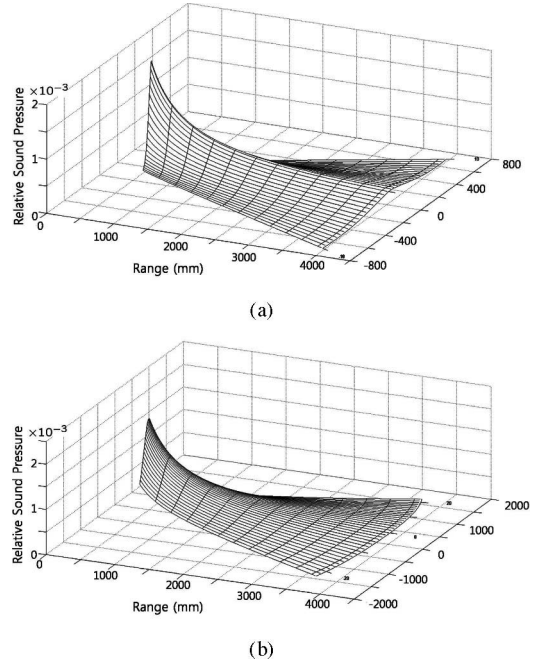


Fig. 8. Transducer sound pressures. These sound pressures are not absolute values as the unknown constants are set to 1. However, this is not important as the constant will be canceled when comparing sound pressure levels. (a) S600. (b) MA50B8.

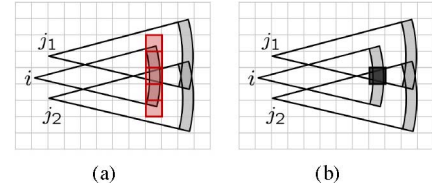


Fig. 9. Conflict cells. (a) Case of five conflict cells. After comparison of the sound pressure, it is concluded that only one cell, which is indicated as the black box in (b), can contain an obstacle. Thus, j_1 and j_2 are incorrect.

In the derivation of (15) and (17), we assume that the excitation frequency f of the sonar sensor is fixed at the value given in the respective manufacturer's data sheet (e.g., 50 kHz for the S600 and 40 kHz for the MA40B8). Different frequencies change the directivity and alter the final detected sound pressure. Therefore, if the sonar sensor is excited at a different frequency, the sound pressure must be recalculated for the appropriate directivity.

2) **Conflict Evaluation Method Using the Sound Pressure**: Let us suppose that conflict cells occur, as shown in Fig. 9(a). In this case, sonar reading i indicates that there may be obstacles in conflict cells, while sonar readings j_1 and j_2 indicate that there are no obstacles. For simplicity, we refer to the former reading (i) as a positive reading and the latter (j_1, j_2) as a negative reading. In addition, if an obstacle exists in a conflict cell, the sound pressure obtained from a positive reading is denoted as SP_P , and the pressure from a negative reading is SP_N . A comparison of SP_P and SP_N leads to the following conclusions.

- 1) $SP_P \geq SP_N$: If there is a real obstacle within the conflict cell, the negative reading can miss it as $SP_P \geq SP_N$.

Hence, under the conservative perspective, it is reasonable to conclude that an obstacle is present.

- 2) $SP_P < SP_N$: If there is a real obstacle within the conflict cell, a negative reading cannot miss it as $SP_P < SP_N$.

Thus, it is reasonable to conclude that no obstacle exists.

In the comparison, the constant c_3 in (15) and (17) is canceled because there is c_3 on both sides of the inequality. In the case of Fig. 9(a), five conflict cells occur as shown in red cells. Assuming the use of MA40B8 transducers, the aforementioned comparison reveals that only the black squared cell of Fig. 9(b) can contain an obstacle. Thus, the sonar readings j_1 and j_2 are incorrect because they have obstacles in their own free regions.

We use this sound pressure comparison to determine whether obstacles exist in conflict cells. This eventually leads to the determination of whether sonar readings are correct. This is the CEsp method, which is used to filter out incorrect readings to ensure there are no longer any conflict cells. After the conflict cells are removed, only consistent or uncertain cells remain. Using this, the ML approach can be converted to a simple logic problem.

IV. MAXIMUM APPROXIMATED LIKELIHOOD APPROACH

When there are no conflict cells, the ML approach can be simplified to a light logic problem of $O(n)$.

A. ML Approach

As sonar sensors were originally designed to provide the distance to the closest obstacle in their beamwidth, their likelihood can be defined as

$$p(z_i|M) = \eta \exp \left\{ -\frac{1}{2} \left(\frac{z_i - d(N_i)}{\sigma} \right)^2 \right\}. \quad (18)$$

where z_i denotes the measurement of the sensor, M is the map, η is a normalizing term, σ is the range uncertainty, and $d(N_i)$ is the distance to the nearest obstacle N_i in the beamwidth, which is defined as

$$d(N_i) = \begin{cases} \text{distance to } N_i, & \text{for } N_i \neq \emptyset \\ z_{\max}, & \text{for } N_i = \emptyset \end{cases}. \quad (19)$$

Although more complicated likelihood was introduced in [11], only (18) is sufficient for building a reliable grid map, as it can handle the angular uncertainty of the sonar sensor, as shown in Section VI.

Based on (18), the ML grid map is acquired through

$$\operatorname{argmax}_M p(Z|M) = \operatorname{argmax}_M \prod_i p(z_i|M) \quad (20)$$

$$= \operatorname{argmax}_M \sum_i \log p(z_i|M) \quad (21)$$

$$= \operatorname{argmin}_M \sum_i (z_i - d(N_i))^2 \quad (22)$$

where $Z = \{z_1, \dots, z_n\}$. On the right-hand side of (20), a static world assumption is used, which indicates that other sensor measurements are conditionally independent when map M is given [1], [11]. The log function is introduced for computational

TABLE I
PERCENTAGES OF INCORRECT READINGS

	Env.	# of Readings	Correct (%)	Incorrect (%)
MA40B8	C#1	75,720	45	55
	C#2	20,808	46	54
	H#1	33,864	50	50
	H#2	17,100	54	46
	H#3	17,856	58	42
	H#4	33,360	58	42
	H#5	26,196	50	50
	Total	224,904	50	50
S600	C#1	97,504	38	62
	C#2	29,296	38	62
	H#1	51,504	38	62
	Total	178,304	38	62

reasons in (21), and the application of simple algebra results in (22). The ML approach is to find the solution that minimizes the sum of quadratic functions. However, it suffers from two critical problems: erroneous map and heavy computational load.

1) *Erroneous Map*: Direct use of sonar measurements does not guarantee good quality ML grid maps because the ML approach suffers from the intrinsic overfitting problem [41]. As approximately 55% of sonar measurements are incorrect (Table I²), the ML grid map will be overfitted to these measurements and contain many errors. The problem, however, can be alleviated using the CEsp method that rejects incorrect measurements.

2) *Heavy Computation*: Finding the solution to (22) is a high-dimensional numerical optimization problem. As a map has 2^k dimensions, the solution requires $O(2^k n)$ computational complexity. The complexity, however, can be reduced to $O(n)$ by approximation after removing conflict cells, as shown next.

B. MAL Approach

Henceforth, we assume that only consistent and uncertain cells exist because conflict cells are removed by the CEsp method. Based on this assumption, we convert the high-dimensional optimization problem to one of simple logic. This requires an approximation of the likelihood.

Although the quadratic function in (22) is exactly minimum when $z_i = d(N_i)$, we approximate the minimization by relaxing the margin $\pm\beta$ for the range uncertainty β shown in Fig. 2, i.e., the single quadratic function of (22) is considered to be minimized when $|z_i - d(N_i)| \leq \beta$, and then, (22) can be converted

²Table I shows the percentages of incorrect readings for the MA40B8 and S600 sonar sensors. Seven and three experiments in different environments were conducted for MA40B8 and S600, respectively, to collect sonar measurements using the experimental setups described in Section VI. We obtained a reference map for each environment that combines a map from a laser sensor with a blueprint of the environment. We determined whether each sonar reading was correct based on the reference map. As the sonar readings have a range of uncertainty and are affected by the estimation error due to the robot's position, we set the range of uncertainty boundary to ± 150 mm, i.e., any reading i with $|z_i - d(N_i)| > 150$ mm is considered to be incorrect. The table shows that about 60% of S600 measurements and 50% of MA40B8 measurements are incorrect. The irregular configuration of S600s results in more spurious measurements than for the MA40B8s. This is also in part due to the larger beamwidth of the MA40B8.

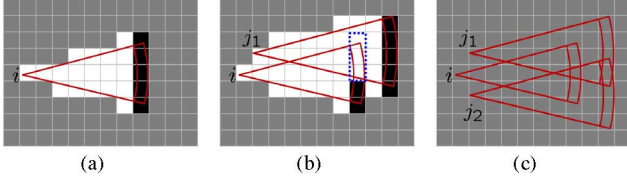


Fig. 10. (a) MAL result for the case of consistent cells. (b) MAL result for the case of consistent and uncertain cells (the uncertain cells are indicated as the blue dotted box). (c) Conflict cells.

to the following:

$$\operatorname{argmin}_M \sum_i (z_i - d(N_i))^2 \approx \operatorname{argmin}_M \sum_i f(i) \quad (23)$$

where $f(i)$ is defined as

$$f(i) = \begin{cases} 0, & \text{for } |z_i - d(N_i)| \leq \beta \\ (z_i - d(N_i))^2, & \text{for } |z_i - d(N_i)| > \beta \end{cases}. \quad (24)$$

Thus, whenever N_i is located in the arc region of a reading, the likelihood of the reading is approximately the maximum.

The global solution to (23) is to minimize all $f(i)$, which can be achieved when the closest obstacle of each sonar measurement is located in the arc region for this measurement. While the global solution is difficult to achieve or requires high-dimensional optimization for general cases, the following theorem shows that the global solution is easily obtainable when there are no conflict cells.

Theorem 2: When conflict cells do not exist, each sonar reading can have its own closest obstacle inside its own arc region.

Proof: As we assume that conflict cells have been removed, it is necessary to examine only two cases: one in which only consistent cells exist (case 1) and the other in which both uncertain and consistent cells exist (case 2). It is impossible for uncertain cells to exist alone.

- 1) *Case 1:* When a sonar reading has only consistent cells, as in Fig. 10(a), it is trivial to determine that the closest obstacle can be located in the arc region of the reading.
- 2) *Case 2:* When a sonar reading has both consistent and uncertain cells, as in Fig. 10(b), obstacles can be located in the arc region. In Fig. 10(b), sonar reading i has uncertain cells in its arc region, but not all cells in the arc region are uncertain. Therefore, without affecting other sonar readings, the sonar reading can have the closest obstacle in its arc region. In addition, sonar reading j_1 has uncertain cells in its free region. As the uncertain cells are not related to the arc region of sonar reading j_1 , it can also have the closest obstacle in its arc region. ■

Theorem 2 indicates that the global solution of (23) is achievable when there are no conflict cells, and the solution can be obtained by the simple logical process, as summarized in Fig. 11. When a cell is consistent, its state is set according to the information it contains. Specifically, if the cell is in an arc region, it is set to the occupied state that corresponds to an obstacle. Conversely, if the cell is in a free region, it is set to the empty state. When a cell is uncertain, the cell is considered empty. If the uncertain cells are set to the occupied state, the quadratic func-

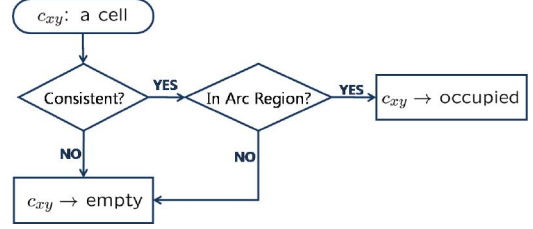


Fig. 11. Summary of the MAL approach. The manner in which consistent cells are set to be the same with the same information and uncertain cells are set to be empty minimizes (23) globally.

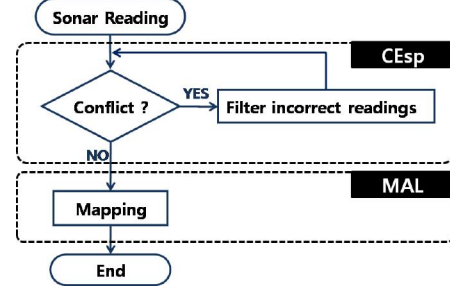


Fig. 12. CEMAL approach flowchart.

tions of the other sensors would increase and not be minimized. For example, setting the uncertain cells of the sonar reading i in Fig. 10(b) to the occupied state increases the quadratic function of the sonar reading j_1 , and the global solution is not possible. We call this simple process the MAL approach, and it has a computational complexity of $O(n)$ because it is just linear with the number of all measurements.

If conflict cells exist, as in Fig. 10(c), the solution that minimizes the quadratic function of the sonar reading i always increases the function of j_1 or j_2 . As we remove all of the conflict cells by the CEsp method, however, it is not necessary to consider this case.

V. METHOD OVERVIEW

The CEsp method and the MAL approach are proposed based on the conflict cell. Integrating the MAL approach with the CEsp method results in the CEMAL approach outlined in Fig. 12. As the CEsp method and the MAL approach can work incrementally, the procedure shown in Fig. 12 is executed once each time a sonar reading occurs. After receiving the sonar reading, the process checks whether conflict cells occur; if so, the CEsp method is executed until no conflict cells remain, and then, the MAL process is executed.

In the worst case, the complexity of the CEMAL approach is $O(n^2)$: $O(n^2)$ for the CEsp method and $O(n)$ for the MAL approach, i.e., the CEsp method dominates the complexity. In one cycle, the CEsp method checks whether the incoming reading causes conflict cells. This check may require that all other readings be checked. This is the worst case, and eventually, the complexity becomes $O(n^2)$. In practice, however, the complexity of the CEsp method is not $O(n^2)$ because once readings are filtered, they are no longer considered. Moreover, the worst

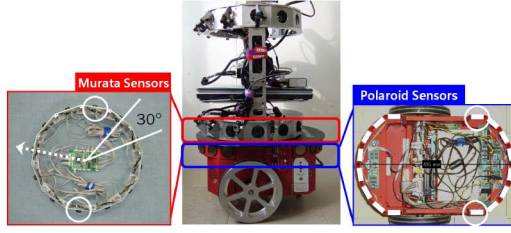


Fig. 13. Configuration of the sonar sensors used in the experiments. The left-hand image shows 12 MA40B8s, with a white dotted arrow indicates the direction of robot travel. In the right-hand figure, each white box represents the position of 16 S600 sensors. The white circles represent the sonar sensors used in the experiments described in Section VI-D.

case only occurs when all sonar readings are accumulated within small areas (e.g., a robot stops in one position for a long time). As the worst case can be avoided with a simple algorithm to prevent the robot from gathering measurements when it stops, the complexity of the CEsp method can be regarded as $O(n)$.

VI. EXPERIMENTAL RESULTS

A. Experimental Setup

We conducted experiments in various indoor environments using both the S600 and MA40B8 sonar sensors to verify the performance of the CEMAL approach. The configurations of the sonar sensors are shown in Fig. 13. Seven experimental environments, which are designated as C#1, C#2, and H#1–5, were used. Environments C#1 and C#2 were corridors, and environments H#1–5 were home-like environments containing general household items, such as tables, chairs, couches, and electronic appliances. The MA40B8 experiments were conducted in all environments, while the S600 was used only in C#1, C#2, and H#1.

The cell size used was $5 \text{ cm} \times 5 \text{ cm}$, and a set of sonar measurements was sampled at a frequency of 4 Hz while the robot moved manually. The translational velocity of the robot was fixed at 150 mm/s and its rotational velocity was $25^\circ/\text{s}$. In addition, the maximum admissible range of the sonar sensor was limited to 4 m because this was sufficient to represent general indoor environments. As localization during mapping was not an issue of concern in this study, we assumed that pose estimations were available, which rely on the extended Kalman-filter-based simultaneous location and mapping (SLAM) [42].

Due to space limitations, only two results for the MA40B8 and the S600, respectively, are illustrated in this paper, while the other results are simply summarized in tables or graphs. All of the map building processes, however, are provided in the multimedia material.

B. CEMAL Approach Versus Conventional Grid Mapping Approaches

We compared the performance of CEMAL with a number of representative grid mapping approaches: the PT, the DS, the FZ, and the ML approach.

As mentioned in Section II, PT, DS, and FZ require regulation of the update parameters. For PT, $p(c_{xy} = O|z_i)$ should be

regulated and is generally defined as

$$p(c_{xy} = O|z_i) = \begin{cases} 0.5 + \frac{A_{PT}\Gamma(\theta)}{2}, & \text{for } c_{xy} \in A(i) \\ 0.5 - \frac{F_{PT}\Gamma(\theta)\Delta(r)}{2}, & \text{for } c_{xy} \in F(i) \end{cases} \quad (25)$$

where c_{xy} denotes a cell, O is the occupied state, z_i is the measurements of sonar reading i , $\Gamma(\theta)$ is a weighting function of θ , $\Delta(r)$ is a weighting function of r , and A_{PT} and F_{PT} are the maximum values for their respective weight functions and will be regulated. The weighting functions are defined as

$$\Gamma(\theta) = 1 - \left(\frac{\theta}{(\theta_W/2)} \right)^2 \quad (26)$$

$$\Delta(r) = 1 - \frac{1 + \tanh(2(r - r_v))}{2} \quad (27)$$

where θ_W is the beamwidth of the sonar sensor, and r_v is the visibility radius for a smooth transition. As the maximum range of a measurement is 4 m, r_v is set to half of this value. For DS, $m(c_{xy} = O)$ and $m(c_{xy} = E)$ should be controlled, and they are generally defined as

$$m(c_{xy} = O) = \begin{cases} A_{DS}\Gamma(\theta), & \text{for } c_{xy} \in A(i) \\ 0, & \text{for } c_{xy} \in F(i) \end{cases} \quad (28)$$

$$m(c_{xy} = E) = \begin{cases} 0, & \text{for } c_{xy} \in A(i) \\ F_{DS}\Gamma(\theta)\Delta(r), & \text{for } c_{xy} \in F(i). \end{cases} \quad (29)$$

In (28) and (29), A_{DS} and F_{DS} are controllable, as they are for PT. For FZ, $\mu_O(c_{xy})$ and $\mu_E(c_{xy})$ should be adjusted, and they are normally defined as

$$\mu_O(c_{xy}) = \begin{cases} A_{FZ}\Gamma(\theta), & \text{for } c_{xy} \in A(i) \\ 0, & \text{for } c_{xy} \in F(i) \end{cases} \quad (30)$$

$$\mu_E(c_{xy}) = \begin{cases} 0, & \text{for } c_{xy} \in A(i) \\ F_{FZ}\Gamma(\theta)\Delta(r), & \text{for } c_{xy} \in F(i) \end{cases} \quad (31)$$

where A_{FZ} and F_{FZ} are adjustable. There is a physical interpretation of these tunable parameters in [14]. Among various parameter candidates, the value that maximizes the correct representation ratio (CRR), which will be described in Section VI-B2, is used to build a grid map.

For DS in particular, a state that has the maximum of three values (occupied, empty, and unknown) is shown. The Dombi operator [23] and the bounded product operator are used with FZ. The EM algorithm is used with the ML approach to reduce the computational burden.

1) *Qualitative Comparison:* We combined data from the LRF with a blueprint of each environment to create accurate reference maps [see Figs. 14–17(a)] because the LRF and the blueprint complement each other. The blueprint compensates for obstacles that the LRF sometimes misses, and the LRF provides detailed information (e.g., furniture and electronic appliances) that the blueprint does not contain.

The results of the binary or trinary estimation approaches (PT, DS, and FZ) are shown in Figs. 14 to 17(b)–(d). Although the

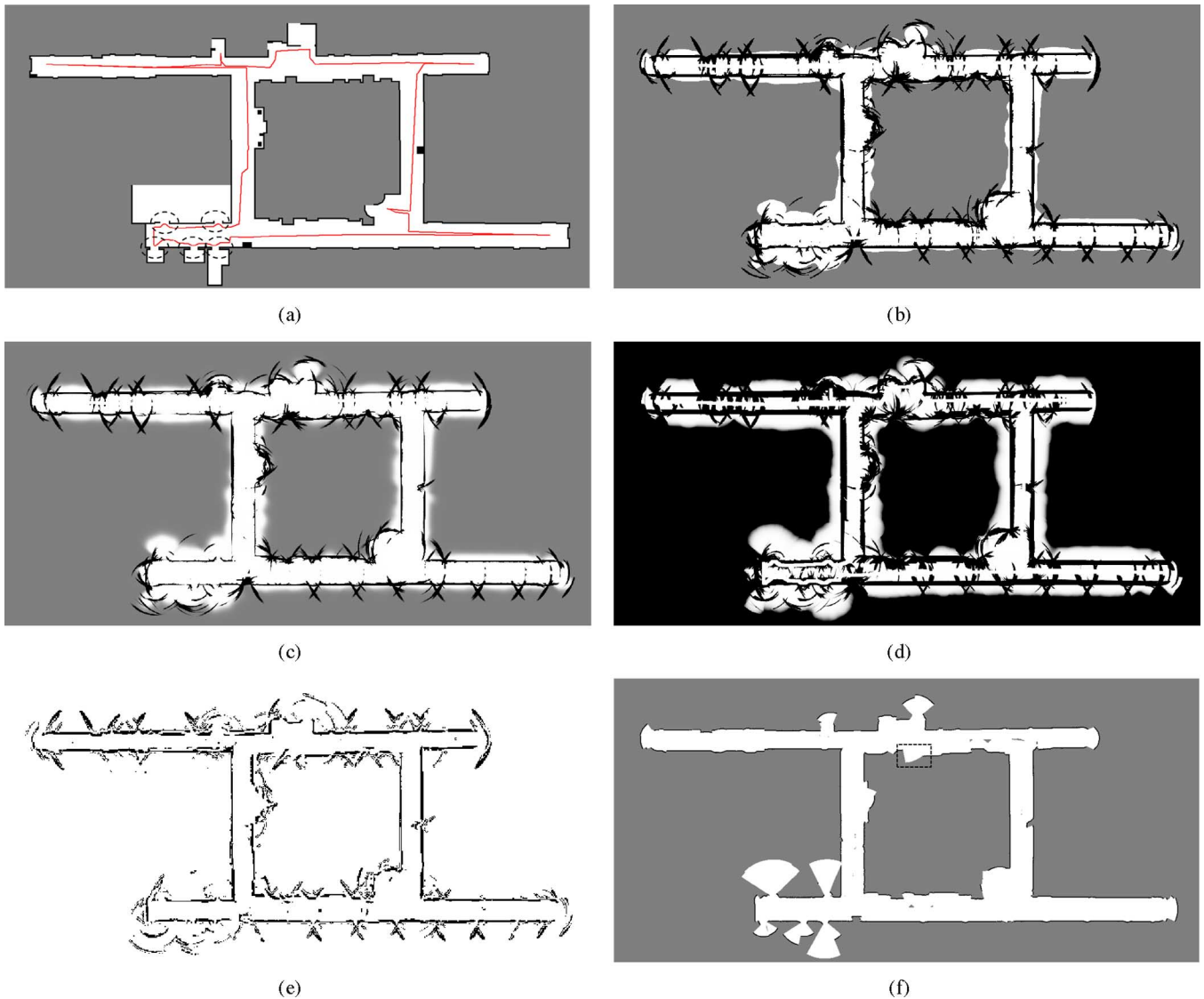


Fig. 14. Experimental results in environment C#1 (62 m \times 30 m) with MA40B8 sensors. (a) Reference map. The line indicates the trajectory of the robot and the dashed areas represent narrow openings. (b) PT map ($A_{PT} = 0.9$, $F_{PT} = 0.4$). (c) DS map ($A_{DS} = 0.9$, $F_{DS} = 0.1$). (d) FZ map ($A_{FZ} = 0.6$, $F_{FZ} = 0.1$). (e) ML map. The ML map contains only occupied and empty cells because the ML approach originally sets the state of a cell to occupied or empty state. (f) CEMAL map. The dashed areas represent significant errors.

overall shape of each environment is captured successfully, it is obvious that the maps still contain errors where areas outside the boundary of the environment are marked as empty. Moreover, in Figs. 14 and 15(b)–(d), we can see that the five narrow openings circled in Figs. 14 and 15(a) are not successfully represented. The failure is the result of improper handling of the angular uncertainty and incorrect measurements. In particular, Fig. 14(b)–(d) shows that parts of the inner area of the environment are repeatedly blocked because the MA40B8 has a wider beamwidth than that of the S600. In Fig. 16(d), the blocking is pronounced because the FZ approach is more conservative in the occupied state. Revising the parameters of each approach to emphasize occupied regions causes previously undetected obstacles to become visible and results in the appearance of ghost obstacles. Revising the parameters in the opposite direction makes ghost obstacles disappear while also causing some

true obstacles to vanish. Thus, these approaches have tradeoffs that make it difficult to represent the environment.

On the other hand, the results of the ML approach shown in Figs. 14–17(e) successfully represent the overall shape of the environment as well as the inner area without any parameter adjustment, even though erroneous parts in the outside area remain. Specifically, in terms of representing the narrow openings, Figs. 14 and 15(e) are not satisfactory because incorrect measurements obstruct a clear representation.

In contrast, Figs. 14–17(f), which are the results of the CEMAL approach, are excellent, compared with the other results in terms of map quality, in that the occupied regions are placed more accurately and the empty regions are shown more clearly. The narrow openings in particular are clearly represented. There are still a few erroneous sections indicated by dashed areas in Figs. 14–17(f), because the CEMAL method does not completely

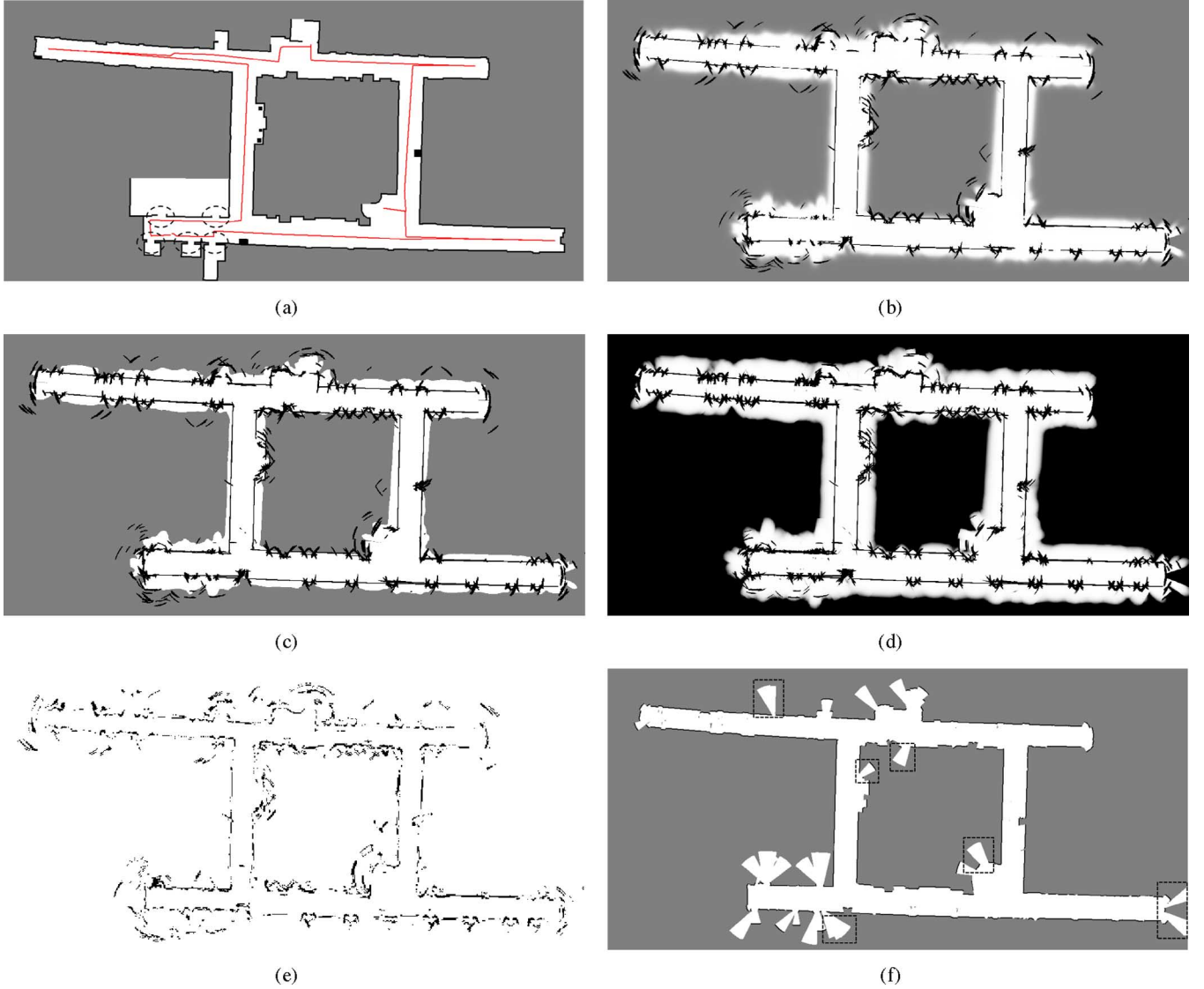


Fig. 15. Experimental results in environment C#1 (62 m \times 30 m) with S600 sensors. (a) Reference map. The line indicates the trajectory of the robot, and the dashed areas indicate narrow openings. (b) PT map ($A_{PT} = 0.9$, $F_{PT} = 0.4$). (c) DS map ($A_{DS} = 0.9$, $F_{DS} = 0.1$). (d) FZ map ($A_{FZ} = 0.9$, $F_{FZ} = 0.1$). (e) ML map. (f) CEMAL map. The dashed areas indicate significant errors.

remove all incorrect measurements. Nevertheless, it is clear that the CEMAL approach has the best ability to represent the environment without adjusting parameters, even with erroneous sonar measurements.

2) *Quantitative Comparison*: We defined two criteria to evaluate and compare the performance of the mapping approaches quantitatively. The first is the CRR, which is a type of reliability measure that indicates the map accuracy. The CRR is given by

$$\text{CRR} = \frac{\# \text{ of correct empty cells in the map being evaluated}}{\# \text{ of all empty cells in the map being evaluated}} \quad (32)$$

where a correct empty cell is a cell that is designated empty in both the reference map and the map being evaluated.

The second criterion is the complete representation ratio (MRR), which shows how much the map succeeds in representing the environment. The MRR is a type of completeness

measure and is given by

$$\text{MRR} = \frac{\# \text{ of correct empty cells in the map being evaluated}}{\# \text{ of all empty cells in the reference map}} \quad (33)$$

Figs. 18 and 19 show that CEMAL has the best performance in terms of CRR and MRR. The CRR results indicate that a CEMAL map is 92% accurate, and the MRR indicates that it represents about 96% of the entire environment. Thus, the CEMAL map is a faithful representation.

3) *Computational Load*: Table II shows the total computation time required to create the map using each approach. The ML approach requires a very long time despite using the EM algorithm, which makes it impractical for actual use. On the other hand, while the CEMAL approach is based on the ML approach, its execution time is comparable with the other estimation approaches. The CEMAL time is somewhat longer because CEMAL is a two-layered approach incorporating a

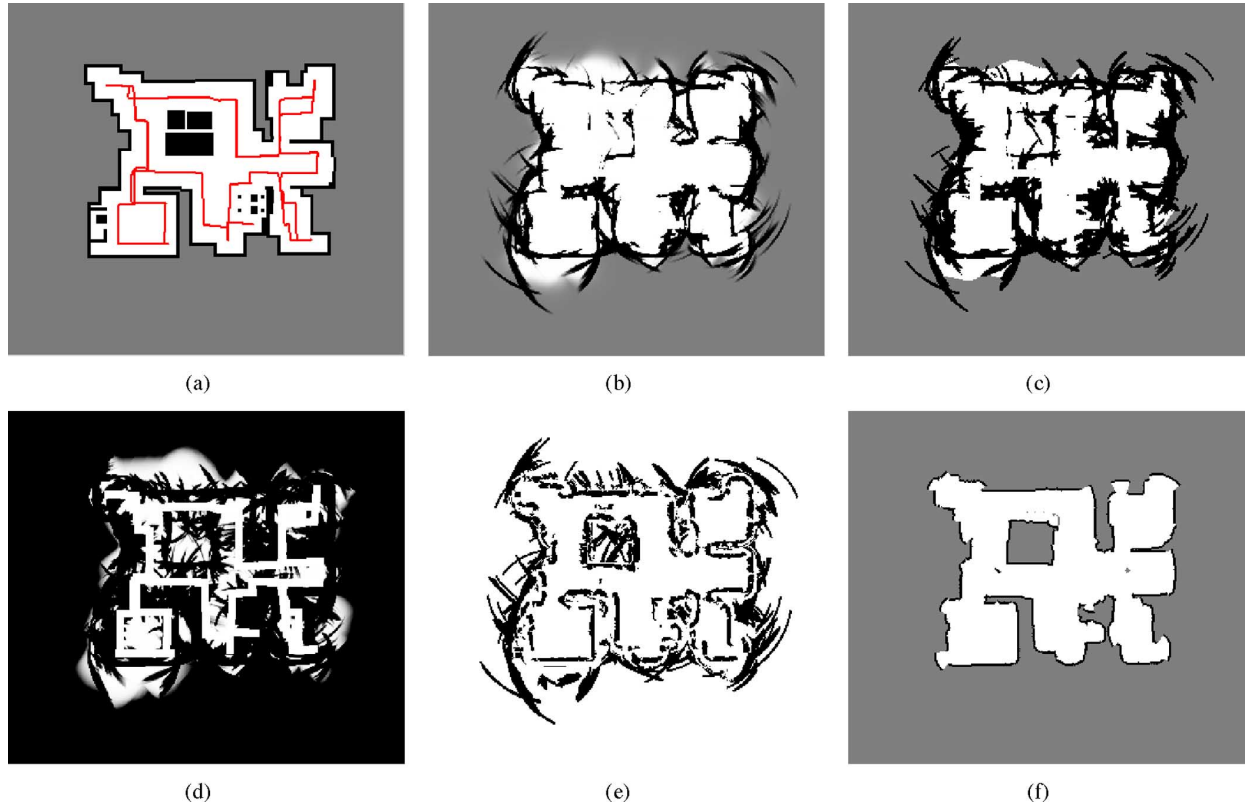


Fig. 16. Experimental results in environment H#1 (18 m \times 16 m) with MA40B8 sensors. (a) Reference map. The line indicates the trajectory of the robot. (b) PT map ($A_{PT} = 0.9, F_{PT} = 0.4$). (c) DS map ($A_{DS} = 0.9, F_{DS} = 0.1$). (d) FZ map ($A_{FZ} = 0.9, F_{FZ} = 0.1$). (e) ML map. (f) CEMAL map.

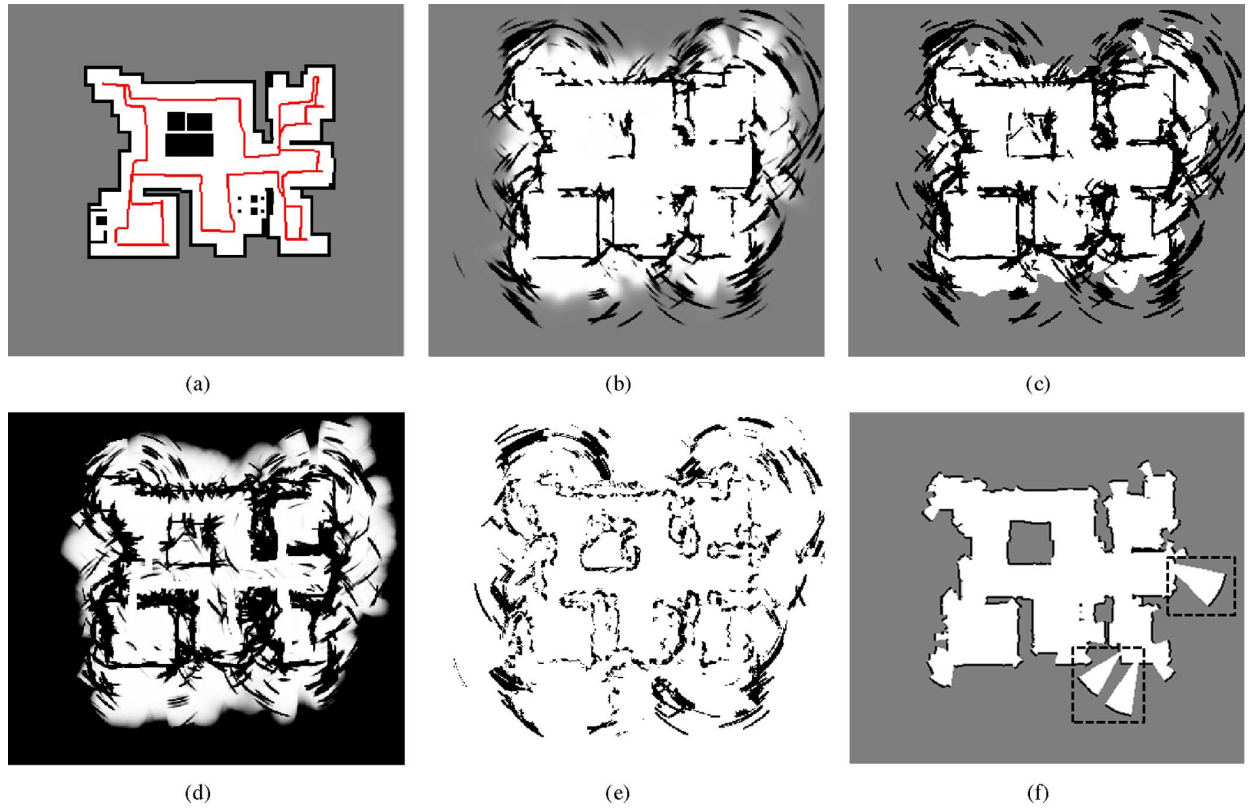


Fig. 17. Experimental results in environment H#1 (18 m \times 16 m) with S600 sensors. (a) Reference map. The line indicates the trajectory of the robot. (b) PT map ($A_{PT} = 0.9, F_{PT} = 0.4$). (c) DS map ($A_{DS} = 0.9, F_{DS} = 0.1$). (d) FZ map ($A_{FZ} = 0.9, F_{FZ} = 0.1$). (e) ML map. (f) CEMAL map. The dashed areas represent significant errors.

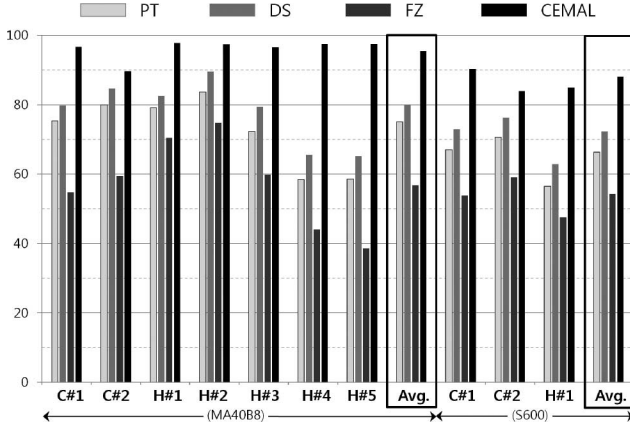


Fig. 18. CRRs for the different approaches. One experiment was conducted for each environment.

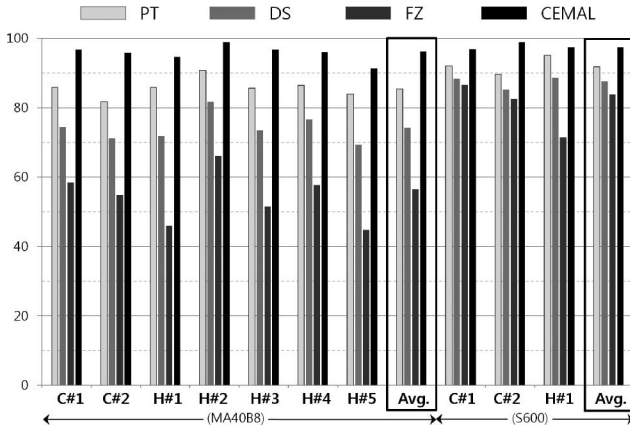


Fig. 19. MRRs for the different approaches. One experiment was conducted for each environment.

filtering layer (CEsp method) and a fusion layer (MAL approach), while PT, DS, and FZ have only a fusion layer. Even though it is longer, the CEMAL execution time is not prohibitive for practical use. Therefore, the CEMAL approach is a good alternative, considering the resulting map quality and the computation time.

Table III shows the mean computation time for a single measurement to confirm the feasibility of the incremental CEMAL approach. The mean time of MA40B8 measurements is longer than that of S600 measurements because of the larger beamwidth. The CEMAL approach requires an average of 1 ms to process a measurement and is thus quite practical for real-time operation.

C. CEMAL Approach Versus Methods for Coping With Sonar Sensor Characteristics

As described in Section II, previous work regarding the sonar sensor characteristics can be grouped into filtering incorrect measurements and handling the angular uncertainty. Therefore, we examined the CEMAL approach using these two considerations.

1) *Filtering Incorrect Measurements:* In Section II, we divided previous work on rejection of incorrect sonar measurements into three classes. For comparison with the CEsp method,

TABLE II
TOTAL COMPUTATIONAL TIME (IN SECONDS)

	Env.	PT	DS	FZ	ML(EM)	CEMAL
MA40B8	C#1	37	38	75	47,500	105
	C#2	9	9	18	11,596	19
	H#1	10	10	22	26,071	38
	H#2	6	6	13	7,346	12
	H#3	4	4	8	9,807	19
	H#4	7	8	17	14,293	34
	H#5	5	5	12	11,506	22
	Avg.	11	12	24	18,303	36
S600	C#1	41	42	72	4,297	81
	C#2	11	11	20	1,258	21
	H#1	15	15	28	7,239	43
	Avg.	22	23	40	4,265	48

OS: Windows XP, CPU: 2.6-GHz Pentium 4; Language: C++; application: single thread application.

TABLE III
MEAN COMPUTATION TIME FOR PROCESSING ONE SONAR MEASUREMENT (IN MILLISECONDS)

	Env.	PT	DS	FZ	CEMAL
MA40B8	C#1	0.5	0.5	1.0	1.4
	C#2	0.4	0.4	0.9	0.9
	H#1	0.3	0.3	0.6	1.1
	H#2	0.3	0.3	0.8	0.7
	H#3	0.2	0.2	0.5	1.1
	H#4	0.2	0.2	0.5	1.0
	H#5	0.2	0.2	0.5	0.9
	Avg.	0.3	0.4	0.7	1.1
S600	C#1	0.4	0.4	0.7	0.8
	C#2	0.4	0.4	0.7	0.7
	H#1	0.3	0.3	0.5	0.8
	Avg.	0.4	0.4	0.7	0.8

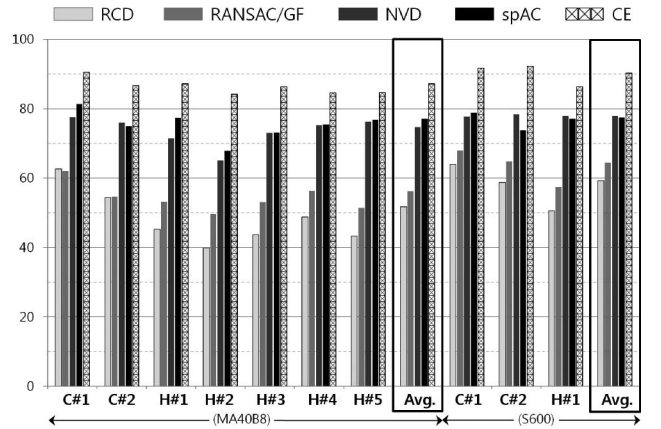


Fig. 20. CDR for the different approaches.

we selected a representative method from each of the four classes: RCD, RANSAC/GF, NVD, and spAC.

It is necessary to determine the actual state of all sonar readings to verify the performance of these methods. Based on the reference map presented in Section VI-B, the state is likely to be incorrect when $|z_i - d(N_i)| > 150$ mm. We created the correct decision ratio (CDR) based on the reference state of all sonar readings to indicate the proportion of measurements correctly determined through a filtering process. CDR is defined as

$$\text{CDR} = \frac{\# \text{ of correctly decided measurements}}{\# \text{ of all measurements}} \times 100. \quad (34)$$

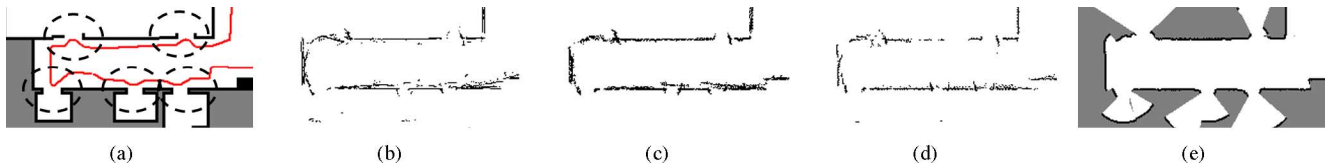


Fig. 21. Lower left-hand portion of the experimental results in environment C#1 (12 m \times 6 m) with MA40B8 sensors. (a) Reference map, where dashed areas represent narrow openings. (b) Arc map produced using the AC method. (c) Arc map produced using the ATM method. (d) Arc map produced using the DM method. (e) CEMAL map.

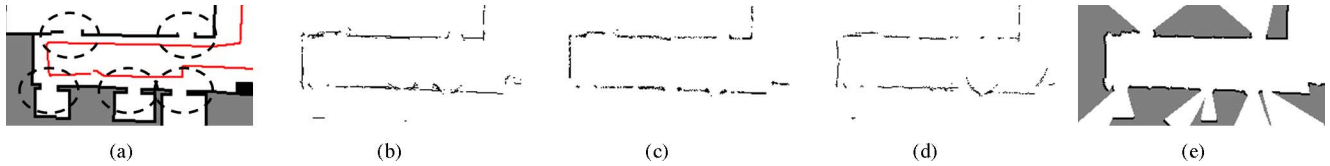


Fig. 22. Lower left-hand portion of experimental results in environment C#1 (12 m \times 6 m) with S600 sensors. (a) Reference map, where dashed areas represent narrow openings. (b) Arc map produced using the AC method. (c) Arc map produced using the ATM method. (d) Arc map produced using the DM method. (e) CEMAL map.



Fig. 23. CEMAL maps in environment C#1 (62 m \times 30 m). (a) With only two MA40B8 sensors. (b) With only two S600 sensors.

The numerator in (34) is the total number of measurements accurately determined to be correct or incorrect.

As shown in Fig. 20, the CEsP method has the best performance for correctly determining the state of measurements, with a CDR of about 88%. This confirms that the CEsP method is useful in practical applications to determine the true state of sonar readings. The spAC method also has relatively good performance compared with the others. As both the CEsP and spAC methods are based on conflict cells, the results show the power of the conflict cell approach in filtering sonar measurements.

2) *Handling Angular Uncertainty*: In general, to deal with the angular uncertainty, an environment is represented by the arc map [29]. The ATM and DM methods show the best performance [30]. We compared the performance of the ATM, DM, and AC methods in representing the narrow openings indicated by dotted circles in Figs. 21 and 22(a), which are shown in the lower left-hand portions of Figs. 14 and 15(a), respectively. We investigated the representation of narrow openings because the management of angular uncertainty is difficult to measure quantitatively. For a fair comparison, only the readings remaining after applying the CEsP method were used.

For the S600, Fig. 22(b)–(e) shows that all methods successfully map the narrow openings. For the MA40B8, which has bigger angular uncertainty than the S600 due to wider beamwidth,

however, the results of the other methods are not satisfactory because some narrow openings are blocked, as shown in Fig. 21(b)–(d). Even with the MA40B8, the CEMAL approach clearly expresses the narrow openings, as shown in Fig. 21(e). These results illustrate that the CEMAL approach can handle the angular uncertainty appropriately and, thus, express narrow openings, regardless of the type of sonar sensor.

D. Use of Only Two Sonar Sensors

For reasons of cost, a low number of sonar sensors is desirable for a commercial service such as a robotic vacuum cleaner. To explore this possibility, only the two sonar sensors shown in Fig. 13 are used for building a grid map with the CEMAL approach. As shown in Fig. 23, the CEMAL approach faithfully represents the overall shape of the environment and shows occupied regions accurately. However, it does omit some empty areas in the inner region of the environment because incorrect measurements are rejected, and there are insufficient sonar measurements to cover the whole area. In other environments, as shown in the multimedia material, results of the CEMAL approach are similar to Fig. 23 in terms of overall representation and partial omission. In future research, we will propose a way to reuse filtered incorrect measurements

when there are insufficient sonar measurements. As a filtered reading is not entirely wrong and part of the reading contains useful information, reprocessing can compensate for a lack of measurements.

It should be noted that the configuration of the sonar sensors may be critical to sonar measurements when using only two sensors. In our experiments, the robot followed the walls, and if its two sonar sensors are located on the front and rear, then almost all sonar measurements would be incorrect due to undesirable reflections (see Fig. 1). Because the CEsp method is designed to select correct measurements, it does not produce usable results when almost all measurements are incorrect. As shown in Fig. 13, sonar sensors on the right and left sides of the robot were used to reduce the proportion of incorrect measurements. Therefore, when only two sonar sensors are used to construct a grid map, their configuration should be carefully considered in order to obtain useful measurements.

VII. CONCLUSION

We began this research by asking what was the maximal level of grid map that could be built by sonar sensors. We started with the ML approach because of its suitability to deal with the angular uncertainty of the sonar sensor. The ML approach, however, has two critical problems: the heavy computational load and erroneous parts. The first of these problems prevents general practical use of the ML approach, and the second severely degrades the quality of the ML grid map.

To overcome the problems of the ML approach, it is essential to eliminate conflict cells by filtering out incorrect measurements that cause them. This led us to the CEsp method using the sound pressure of the sonar sensor. After removing conflict cells by the CEsp method, the high-dimensional optimization problem could be converted to the MAL approach. Integrating the MAL approach with the CEsp method results in the CEMAL approach.

The CEMAL approach has computational complexity of $O(n)$, which is very low compared with that of the ML approach $O(2^k n)$ and comparable with those of the binary or trinary estimation approaches [both $O(n)$]. In addition, because the CEsp method rejects most of the incorrect measurements, the quality of the CEMAL grid map is quite high, even using cheap sonar sensors. In situations where the number of sonar readings may not be sufficient, the CEMAL grid map faithfully represents the environment. Furthermore, when acquiring an accurate map, the CEMAL approach does not require parameter adjustment if a fixed type of sonar sensor is used, even though parameters of binary or trinary estimation approaches require tuning whenever a different environment is used for building a grid map, even when the type of the sensor is fixed. Several indoor experiments confirmed that the CEMAL approach is a good compromise between the quality of the map it produces and the computational complexity it entails. In addition, the CEsp method is better than existing methods at determining the true state of sonar measurements. It can be useful for other sonar sensor applications, such as localization and obstacle avoidance, because it is simple and effective.

There are two aspects of our study that should be noted. First, we assumed that pose estimations are available. If the level of pose estimation error is excessive, the quality of the CEMAL grid map cannot be guaranteed. In our experiments, the maximum error between the real final pose and the estimated final pose was approximately 10 cm in both the x - and y -directions. Second, we did not consider the case of moving obstacles. All experiments were conducted in a static environment.

In future research, we will extend the concept of using sound pressure and apply it to handling all inconsistent cells—not just conflict cells. Such an extension may increase the quality of the map and the filtering performance, and the upgraded map will be used for SLAM based on scan matching [43] or map matching [44].

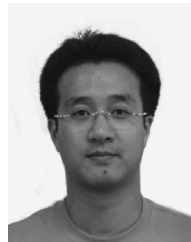
ACKNOWLEDGMENT

The authors would like to thank Y. Byun for helping to implement the proposed method.

REFERENCES

- [1] S. Thrun, W. Burgard, and D. Fox, *Probabilistic Robotics*. Cambridge, MA: MIT Press, 2002.
- [2] D. Fox, W. Burgard, and S. Thrun, "Markov localization for mobile robots in dynamic environments," *J. Artif. Intell. Res.*, vol. 11, pp. 391–427, 1999.
- [3] H. Choset, K. M. Lynch, S. Hutchinson, G. Kantor, W. Burgard, L. E. Kavraki, and S. Thrun, *Principle of Robot Motion: Theory, Algorithms, and Implementations*. Cambridge, MA: MIT Press, 2005.
- [4] R. Siegwart and I. R. Nourbakhsh, *Autonomous Mobile Robots*. Cambridge, MA: MIT Press, 2004.
- [5] W. Lee, H. Ryu, G. Yang, H. Kim, Y. Park, and S. Bang, "Design guidelines for map-based human–robot interfaces: A colocated workspace perspective," *Int. J. Ind. Ergonom.*, vol. 37, no. 5, pp. 589–604, 2007.
- [6] O. Cohen, Y. Edan, and E. Schechtman, "Statistical evaluation method for comparing grid map based sensor fusion algorithms," *Int. J. Robot. Res.*, vol. 25, no. 2, pp. 117–133, 2006.
- [7] D. Silver, D. Morales, L. Rekleitis, B. Lisien, and H. Choset, "Arc carving: Obtaining accurate, low latency maps from ultrasonic range sensors," in *Proc. IEEE Int. Conf. Robot. Autom.*, 2004, pp. 1554–1561.
- [8] M. Hebert, "Active and passive range sensing for robotics," in *Proc. IEEE Int. Conf. Robot. Autom.*, 2000, pp. 102–110.
- [9] H. Choset, K. Nagatani, and N. Lazar, "The arc-transversal median algorithm: A geometric approach to increasing ultrasonic sensor azimuth accuracy," *IEEE Trans. Robot. Autom.*, vol. 19, no. 3, pp. 513–521, Jun. 2003.
- [10] L. Kleeman and R. Kuc, "Sonar sensing," in *Handbook of Robotics*, B. Siciliano and O. Khatib, Eds. New York: Springer-Verlag, 2008.
- [11] S. Thrun, "Learning occupancy grid maps with forward sensor models," *Auton. Robots*, vol. 15, pp. 111–127, 2003.
- [12] P. J. McKerrow and S. M. Zhu, "Modelling multiple reflection paths in ultrasonic sensing," in *Proc. IEEE/RSJ Int. Conf. Intell. Robots. Syst.*, 1996, pp. 284–291.
- [13] D. Bank and T. Kampke, "High-resolution ultrasonic environment imaging," *IEEE Trans. Robot.*, vol. 23, no. 2, pp. 370–381, Apr. 2007.
- [14] M. Ribo and A. Pinz, "A comparison of three uncertainty calculi for building sonar-based occupancy grids," *Robot. Auton. Syst.*, vol. 35, pp. 201–209, 2001.
- [15] H. P. Moravec, "Sensor fusion in certainty grids for mobile robots," *AI Mag.*, vol. 9, no. 2, pp. 61–74, Jul./Aug. 1988.
- [16] S. Thrun, "Learning metric-topological maps for indoor mobile robot navigation," *Artif. Intell.*, vol. 99, no. 1, pp. 21–71, 1998.
- [17] J. Borenstein and Y. Koren, "Histogramic in-motion mapping for mobile robot obstacle avoidance," *IEEE Trans. Robot. Autom.*, vol. 7, no. 4, pp. 535–539, Aug. 1991.
- [18] R. R. Murphy, *Introduction to AI Robotics*. Cambridge, MA: MIT Press, 2000.

- [19] D. Pagac, E. M. Nebot, and H. F. Durrant-Whyte, "An evidential approach to map-building for autonomous vehicles," *IEEE Trans. Robot. Autom.*, vol. 14, no. 2, pp. 623–629, Aug. 1998.
- [20] R. R. Murphy, "Dempster-Shafer theory for sensor fusion in autonomous mobile robots," *IEEE Trans. Robot. Autom.*, vol. 14, no. 2, pp. 197–206, Apr. 1998.
- [21] J. Carlson, R. R. Murphy, S. Christopher, and J. Casper, "Conflict metric as a measure of sensing quality," in *Proc. IEEE Int. Conf. Robot. Autom.*, 2005, pp. 2032–2039.
- [22] G. Oriolo, G. Ulivi, and M. Vendittelli, "Fuzzy maps: A new tool for mobile robot perception and planning," *J. Robot. Syst.*, vol. 14, no. 3, pp. 179–197, 1997.
- [23] G. Oriolo, G. Ulivi, and M. Vendittelli, "Real-time map building and navigation for autonomous robots in unknown environments," *IEEE Trans. Syst., Man, Cybern. B, Cybern.*, vol. 28, no. 3, pp. 316–333, Jun. 1998.
- [24] S. Noykov and C. Roumenin, "Occupancy grids building by sonar and mobile robot," *Robot. Auton. Syst.*, vol. 55, no. 2, pp. 162–175, 2007.
- [25] G. Shafer, *A Mathematical Theory of Evidence*. Princeton, NJ: Princeton Univ. Press, 1976.
- [26] L. A. Zadeh, "Outline of a new approach to the analysis of complex systems and decision process," *IEEE Trans. Syst., Man, Cybern.*, vol. SMC-3, no. 1, pp. 28–44, Jan. 1973.
- [27] K. Pathak, A. Birk, J. Poppinga, and S. Schwertfeger, "3d forward sensor modeling and application to occupancy grid based sensor fusion," in *Proc. IEEE/RSJ Int. Conf. Intell. Robots. Syst.*, 2007, pp. 2059–2064.
- [28] A. P. Dempster, N. M. Laird, and D. B. Rubin, "Maximum likelihood from incomplete data via EM algorithm," *J. R. Stat. Soc. Series B (Methodol.)*, vol. 39, no. 1, pp. 1–38, 1977.
- [29] D. Baskent and B. Barshan, "Surface profile determination from multiple sonar data using morphological processing," *Int. J. Robot. Res.*, vol. 18, no. 8, pp. 788–808, 1999.
- [30] B. Barshan, "Directional processing of ultrasonic arc maps and its comparison with existing techniques," *Int. J. Robot. Res.*, vol. 26, no. 8, pp. 797–820, 2007.
- [31] A. Burguera, Y. Gonzalez, and G. Oliver, "Sonar scan matching by filtering scans using grids of normal distributions," in *Proc. Int. Conf. Intell. Auton. Syst.*, 2008, pp. 64–73.
- [32] M. A. Fischler and R. C. Bolles, "Random sample consensus: A paradigm for model fitting with application to image analysis and automated cartography," *Commun. ACM*, vol. 24, no. 6, pp. 381–395, 1981.
- [33] R. Kuc and M. Siegel, "Physically-based simulation model for acoustic sensor robot navigation," *IEEE Trans. Pattern Anal. Mach. Intell.*, vol. PAMI-9, no. 6, pp. 766–778, Nov. 1987.
- [34] J. J. Leonard and H. F. Durrant-Whyte, *Directed Sonar Sensing for Mobile Robot Navigation*. Boston, MA: Kluwer, 1992.
- [35] S. O'Sullivan, J. J. Collins, M. Mansfield, D. Haskett, and M. Eaton, "Linear feature prediction for confidence estimation of sonar readings in map building," in *Proc. Int. Symp. Artif. Life Robot.*, 2004, pp. 1–4.
- [36] E. Ivanjko, I. Petrovic, and K. Macek, "Improvements of occupancy grid maps by sonar data corrections," presented at the FIRA Robot Soccer World Congr., Vienna, Austria, 2003.
- [37] K. Lee and W. K. Chung, "Navigable Voronoi diagram: A local path planner for mobile robots using sonar sensors," in *Proc. IEEE/RSJ Int. Conf. Intell. Robot. Syst.*, 2007, pp. 2813–2818.
- [38] A. Burguera, Y. Gonzalez, and G. Oliver, "Probabilistic sonar filtering in scan matching localization," in *Proc. IEEE/RSJ Int. Conf. Intell. Robot. Syst.*, 2007, pp. 4158–4163.
- [39] K. Lee, I. H. Suh, S. Oh, and W. K. Chung, "Conflict evaluation method for grid maps using sonar sensors," in *Proc. IEEE/RSJ Int. Conf. Intell. Robots. Syst.*, 2008, pp. 2908–2914.
- [40] L. E. Kinsler, A. R. Frey, A. B. Coppens, and J. V. Sanders, *Fundamentals of Acoustics*. New York: Wiley, 2000.
- [41] C. M. Bishop, *Pattern Recognition and Machine Learning*. New York: Springer-Verlag, 2007.
- [42] S. Ahn, J. Choi, N. L. Doh, and W. K. Chung, "A practical approach for EKF-SLAM in an indoor environment: Fusing ultrasonic sensors and stereo camera," *Auton. Robots*, vol. 24, no. 3, pp. 315–335, 2008.
- [43] A. Burguera, Y. Gonzalez, and G. Oliver, "The likelihood field approach to sonar scan matching," in *Proc. IEEE/RSJ Int. Conf. Intell. Robots. Syst.*, 2008, pp. 2977–2982.
- [44] M. Bosse and R. Zlot, "Map matching and data association for large-scale two-dimensional laser scan-based slam," *Int. J. Robot. Res.*, vol. 27, no. 6, pp. 667–691, 2008.



Kyoungmin Lee received the B.S. and M.S. degrees in mechanical engineering in 2003 and 2005, respectively, from Pohang University of Science and Technology, Pohang, Korea, where he is currently working toward the Ph.D. degree.

His current research interests include the areas of mobile robot navigation, mapping, localization, and integrated exploration.



Wan Kyun Chung (S'84–M'86) received the B.S. degree in mechanical design from Seoul National University, Seoul, Korea, in 1981 and the M.S. degree in mechanical engineering and the Ph.D. degree in production engineering from the Korea Advanced Institute of Science and Technology, Daejeon, Korea, in 1983 and 1987, respectively.

In 1987, he joined Pohang University of Science and Technology, Pohang, Korea, where he is currently a Professor with the School of Mechanical Engineering. During 1988, he was a Visiting Professor with the Robotics Institute, Carnegie Mellon University, Pittsburgh, PA. During 1995, he was a Visiting Scholar with the University of California, Berkeley. His current research interests include the localization and navigation of mobile robots, underwater robots, and the development of robust controllers for precision motion control. He is the Director of the National Research Laboratory for Intelligent Mobile Robot Navigation, Pohang University of Science and Technology, Pohang, Korea. He is a member of the International Editorial Board of *Advanced Robotics*.

Prof. Chung is an Editor of the IEEE TRANSACTIONS ON ROBOTICS.